Total cross section and resonance spectroscopy for $n + {}^{86}Kr$

R. F. Carlton
Middle Tennessee State University, Mufreesboro, Tennessee 37132

R. R. Winters, C. H. Johnson, N. W. Hill, and J. A. Harvey
Oak Ridge National Laboratory, Oak Ridge, Tennessee 37831
(Received 29 March 1988)

The neutron total cross section for $n + {}^{86}Kr$ has been measured over the incident neutron energy range 0.015 to 25 MeV. The average total cross section is obtained for neutron energies from 1 to 25 MeV. For the energy region from 0.015 to 1 MeV, an R-matrix analysis yields resonance parameters which provide a complete representation of the neutron scattering functions for the $s_{1/2}$, $p_{1/2}$, and $p_{3/2}$ scattering channels. From this analysis level densities, neutron strength functions, and external R functions are obtained for the 1-MeV energy region just above the neutron separation energy. The backshifted Fermi-gas model provides excellent descriptions of the level densities for the $\frac{1}{2}^+$, $\frac{1}{2}^-$, and $\frac{3}{2}^-$ states. Evidence of intermediate structure is found for the s-, p-, and d-wave scattering channels.

I. INTRODUCTION

Nuclear structure in the neutron "resonance" region, which corresponds to excitation energies just above the neutron separation energy, can be explored experimentally with good energy resolution by time-of-flight methods. One pressing need[1,2] in nuclear modeling is improvement in level density formulation. Very reliable level densities can be obtained for energies just above the neutron separation energy by transmission measurements with high resolution. For some nuclides one can also measure these densities by observing β decay and delayed neutron emission spectra from radioactive progenitors; however, those techniques usually suffer from relatively poor energy resolution. A comparison of the various types of measurements was a primary motivation for an earlier $n + {}^{86}Kr$ transmission measurement,[3] which was performed at this laboratory using the same sample as used here. The analysis of those data extended up to a neutron energy of 0.4 MeV; the present measurements on $n + {}^{86}Kr$ are made with better resolution so that the resonance analysis can be extended upward to nearly 1 MeV.

A unique feature of high-resolution measurements is that neutron-scattering functions can be extracted for individual partial waves, i.e., for s, p, and in some cases d waves. Often, such as the present case, the scattering functions for the first few partial waves can be deduced from high-resolution transmission data alone, without additional differential scattering data, because the interference patterns are distinctive for each partial wave. Such favorable cases require nuclides with relatively large level spacings such that resonances can be resolved over an energy region of several hundred keV. With present techniques that is possible for nuclides in three regions of the Periodic Table, namely, for some light nuclides with $A < 60$ and for nuclides near the 50- and 126-neutron closed shells. The ^{86}Kr target is one of the four stable spin-zero nuclides which have 50 neutrons.

One interest in nuclides near the 50-neutron closed shell is that, since their masses are near the $3p$ size resonance,[4] they present the possibility of measuring spin-orbit effects in the resonance region. There is abundant empirical evidence for a spin-orbit potential, not only from scattering and polarization measurements for higher neutron energies but also from data at negative energies, where a spin-orbit term is crucial for the shell-model interpretation of the bound states. In the resonance region, one would expect spin-orbit effects to be observed in the splitting of the $3p$ size resonance. However, the splitting is not observed because the spreading widths of the $p_{1/2}$ and $p_{3/2}$ components exceed their energy separation. In a recent work,[5] the splitting of the size resonance was observed by measuring scattering angular distributions with poor resolution. Those authors concluded, from a survey of earlier high-resolution measurements, that the spin-orbit effects could not be observed from such measurements, even with the best possible energy resolution. An alternative conclusion is that the earlier measurements covered too small energy regions to include a statistically meaningful number of p-wave resonances. A significant number of p-wave resonances can be observed for $n + {}^{86}Kr$ because of the relatively large level spacing and the large p-wave strength function. In the earlier measurement[3] at this laboratory for energies up to 0.4 MeV, the $p_{3/2}$ strength function was found to be larger than that for $p_{1/2}$, as expected from the spin-orbit splitting of the $3p$ orbital. In the present work the measurements and analysis are extended to ≈ 1 MeV.

Once the detailed scattering functions have been obtained for the first few partial waves, they can be individually averaged over energy for comparison to the scatter-

ing functions from an optical model. An additional reason for studying a closed-shell nucleus is that the neutron bound-state structure is relatively simple. A unified mean-field description of both the bound and unbound regions can be accomplished by invoking the dispersion relation constraint[6] This mean-field description is the subject of Ref. 7.

In the present paper we discuss the measurement and analysis of the neutron total cross section for ^{86}Kr. In Sec. II we describe the experiment and report the experimental results, which include not only the detailed cross sections in the resonance region up to 1 MeV but also the averaged cross section for energies up to 25 MeV. In Sec. III we describe the R-matrix analysis of the resonance data and present the resulting parameters of the scattering functions. In Sec. IV we discuss the energy averaged scattering functions and describe the level densities for $J^{\pi}=\frac{1}{2}^{+}$, $\frac{1}{2}^{-}$, and $\frac{3}{2}^{-}$ by use of the backshifted Fermi gas model. Some of the d-wave properties are also discussed in Sec. IV. In Sec. V we discuss possible doorway states in the s-, p-, and d-wave scattering channels and, in Sec. VI, we state our conclusions.

II. MEASUREMENTS

Using the Oak Ridge Electron Linear Accelerator (ORELA) to produce a pulsed neutron beam, we measured the neutron transmission for a gas sample of ^{86}Kr through the resonance region, 15 keV to ≈ 1 MeV, where the energy resolution of ORELA is sufficiently good to allow resonance analysis. At the same time we also measured the transmission with good energy resolution from 1 to 25 MeV, but we present those results only in terms of the average total cross section.

A. The ^{86}Kr sample

The sample was approximately 3.4 g of enriched (99.5%) ^{86}Kr gas contained in a thin wall (0.12 mm) stainless-steel cylinder of 1.08 cm diameter and 30.2 cm length. This cell and an identical empty cylinder were alternated into and out of the neutron beam with a cycle time of approximately 10 min. The empty cell compensated for the transmission of the end walls of the container. Since the sample thickness could be found only approximately from the area and weight, its precise thickness $n=0.0208\pm0.0003$ atoms/b) was determined by the requirement that the peak-to-valley cross section of the large isolated resonance at 137 keV agree with that for an isolated s-wave resonance.

B. Neutron source and detector

At the ORELA facility a burst of 120–150 MeV electrons impinges on a tantalum target and neutrons are produced by the photoneutron process. For the present measurements the electron beam was pulsed at 800 bursts/s with a nominal burst width of 6 ns for a total running time of four weeks. A neutron beam was produced by placing a 0.95 cm collimator at 10 m from the Ta target such as to select the higher energy portion of the photoneutron spectrum, rather than the lower energy part which comes from the water moderator at the source. Two filters were placed in the beam, 3 cm of uranium to attenuate γ rays and a thin ^{10}B filter to remove very slow neutrons that would otherwise overlap the succeeding neutron burst.

The neutron detector was placed at 201.578 ± 0.029 m from the neutron source; the uncertainty[8] includes that arising from the detector's effective thickness. Neutron detection was by proton recoil in an NE110 scintillator coupled to two 8854 RCA photomultiplier tubes operated in coincidence. The scintillator was 2.54 cm thick in the neutron beam direction, 8.75 cm high and 5.16 cm wide along the photomultiplier tubes' axis. Four separate pulse height spectra were recorded with different lower-level discriminator settings. These settings, which corresponded to neutron energies of about 0, 0.4, 0.7, and 2.2 MeV, limited the counting of pulses from late light in the scintillator and also facilitated the measurements of the various backgrounds. The backgrounds were very small; the only correction necessary was a small ($<1\%$) subtraction of room background. The correction for the 1104 ns dead time of the analyzer was about 10% for 1 MeV neutrons and much less for lower energies.

C. Energy resolution

A digital time-analyzer was used to measure the arrival time of each detected neutron to within 1 nsec relative to the arrival of the γ-ray burst from the ORELA target. The neutron energy resolution function has two components. One component arises from the uncertainty ΔL in flight path due to fluctuations in the positions at which neutrons are produced in the ORELA target and are observed in the detector. The other component is due to the finite-time width ΔT of the electron beam burst. The beam width ΔT was measured by including with each sample in-out cycle a brief time-of-flight measurement for which the detector gate was opened in order to record the γ-ray burst; additional U filters were inserted in the beam such that the deadtime was negligible. The sum of such spectra over several hours gave the effective ΔT. The relative uncertainty in the neutron energy, $\Delta E/E$, is expected to be a combination in quadrature of the contributions from ΔL and ΔT,

$$(\Delta E/E)^2=(2\Delta L/L)^2+(2\Delta T/T)^2 \tag{2.1}$$

and has an approximately Gaussian shape. The full width ΔE at half maximum (FWHM) of the Gaussian is given in terms of the uncertainties (FWHM) in neutron flight path length, $\Delta L=2.9$ cm, and flight time, $\Delta T=6$ ns, by

$$(\Delta E/E)^2=(a+bE)\times10^{-8}\ , \tag{2.2}$$

where $a=8.4$ and $b=68$ MeV^{-1}. More nearly complete discussions of experimental details of ORELA transmission measurements are found in Refs. 8–11.

D. Cross sections

The transmission, $T(E)$, was measured for 48 000 time channels corresponding to neutron energies from 0.015 to

25 MeV. The total neutron cross section, $\sigma_T(E)$, is found from the relation

$$T(E)=\exp(-n\sigma_T) \ . \tag{2.3}$$

Figures 1 and 2 present the results for $E<1$ MeV, i.e., the energy region in which the energy resolution and the multilevel structure are such as to allow an R-matrix analysis. The statistical uncertainties are less than the symbol heights. The points plotted near the very narrow resonances represent the observed cross section, but the points in regions where the cross section varies more slowly represent energy averages of the original data. Our reasons for averaging are to facilitate the R-matrix analysis and to improve the visual presentation in the figure. The smooth curves represent the R-matrix parametrization which is discussed in the next section.

The present measurements also extend to energies well above 1 MeV. In fact, data were collected in approximately 10^4 1 ns channels for $1<E<8$ MeV and in 430 6 ns channels for $8<E<25$ MeV. At these energies the multilevel structure is too complex for an R-matrix analysis; nevertheless, these data provide a firm basis for deducing the energy-averaged cross section, $\langle\sigma_T(E)\rangle$. The histogram in Fig. 3 represents $\langle\sigma_T(E)\rangle$ deduced by averaging over energy intervals which were selected to yield a relatively smooth plot. The fluctuations are due to the statistical uncertainties associated with the measurement. For energies up to several MeV the averages presented in Fig. 3 are more accurate than could be obtained from measurements of averaged transmissions by an experiment with poor energy resolution. In such measurements one must assume that the average quantities, $\langle T(E)\rangle$ and $\langle\sigma_T(E)\rangle$, are related in the same manner [Eq. (2.3)] as are $T(E)$ and $\sigma_T(E)$. However, that is a good approximation only if $n\sigma_T$ varies slowly with energy.[12]

III. R-MATRIX ANALYSIS

A. R-matrix formalism

For the present case of a spin 0 nuclide with negligible absorption, the scattering function, $S_{lJ}(E)$, for a given orbital, l, and total angular momentum, J, can be expressed in terms of a real phase shift, $\delta_{lJ}(E)$,

$$S_{lJ}(E)=\exp[2i\delta_{lJ}(E)] \ . \tag{3.1}$$

The neutron total cross section for a given lJ is related to the scattering function,

$$\sigma_{lJT}(E)=(2\pi/k^2)g_J\{1-\mathrm{Re}[S_{lJ}(E)]\} \ , \tag{3.2}$$

or to the real phase shifts,

$$\sigma_{lJT}(E)=(4\pi/k^2)g_J\sin^2[\delta_{lJ}(E)] \ , \tag{3.3}$$

where g_J is the statistical spin factor and k is the neutron wave number. To fit the data we parametrize the phase shifts using the R-matrix[13] formalism,

$$\delta_{lJ}(E)=\varphi_l(E)+\tan^{-1}[P_l(E)R_{lJ}(E)] \ , \tag{3.4}$$

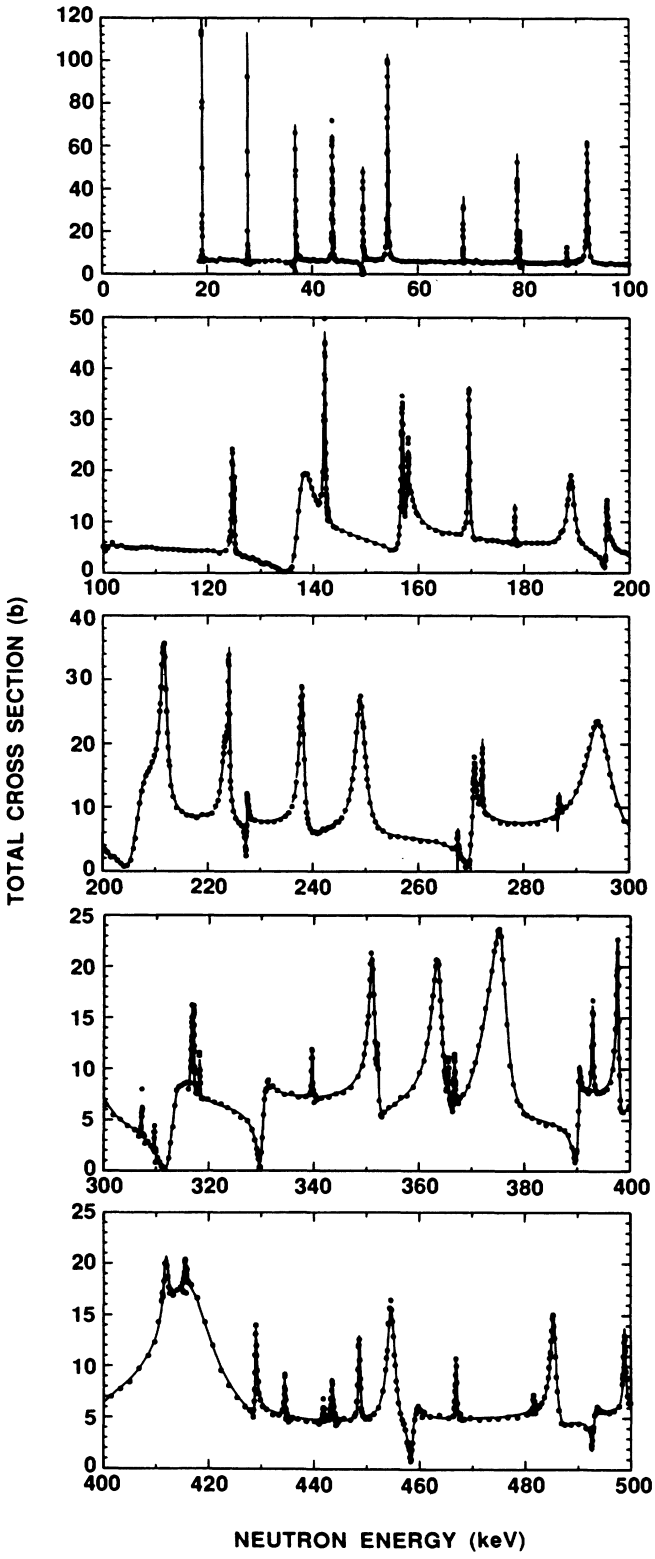

FIG. 1. Total cross section for $n+{}^{86}$Kr. The points represent the measured cross section over the interval 18 to 500 keV. Between resonances the cross sections have been averaged in order to facilitate analysis of the data. The curve represents the multilevel R-matrix description using the parameters in Tables I–III and the boundary radius $a_c=1.45A^{1/3}$.

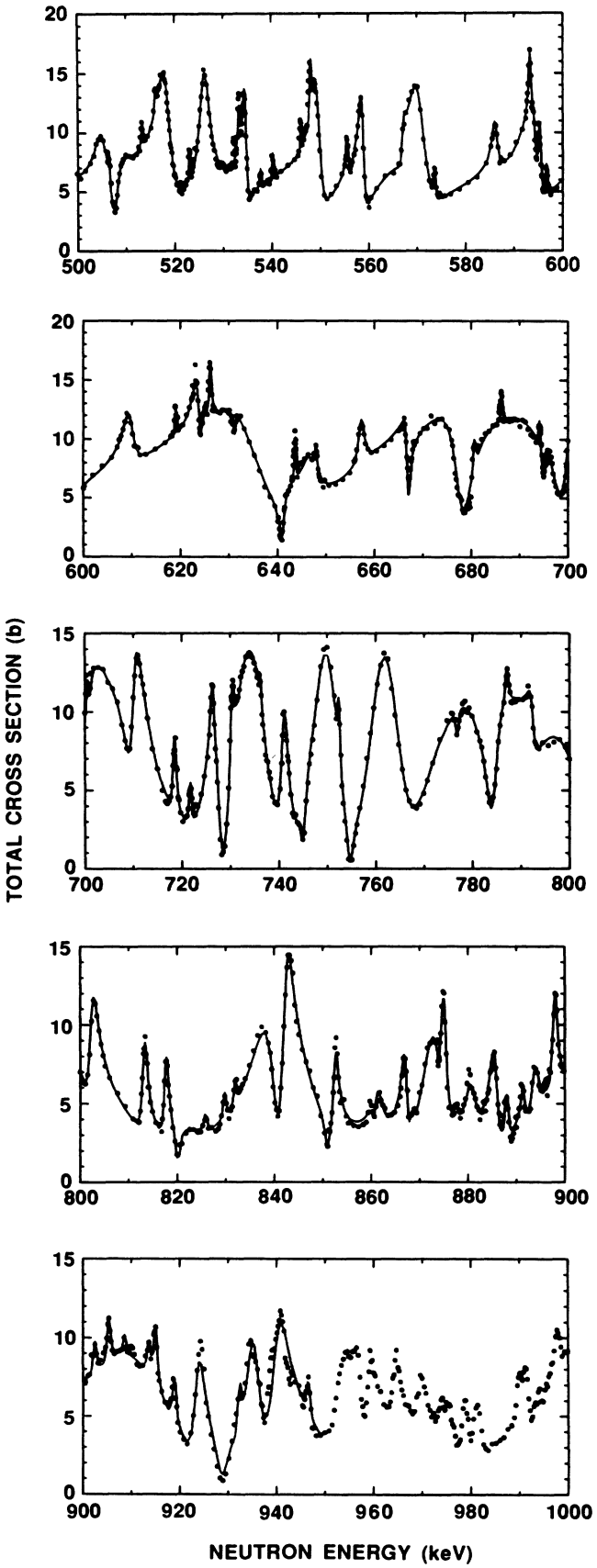

FIG. 2. Same as for Fig. 1 except the energy interval is 500 to 1000 keV.

where we have set the boundary conditions equal to the shift factors at all energies and where P_l and φ_l are, respectively, the l-wave penetrability and hard-sphere phase shift evaluated at the channel radius, taken in this work to be

$$a_c = 1.45 A^{1/3} \text{ fm} . \tag{3.5}$$

The R function is a sum over all the observed resonances plus a smoothly increasing function of energy which describes the aggregate effect of levels external to the region of measurement,

$$R_{lJ}(E) = \sum_{\lambda} \gamma^2_{lJ\lambda}/(E_{lJ\lambda} - E) + R^{\text{ext}}_{lJ}(E) , \tag{3.6}$$

where $\gamma^2_{lJ\lambda}$ and $E_{lJ\lambda}$ are free parameters representing the reduced width and energy of the λth resonance with angular momentum l and J.

The external R function, R^{ext}, is to be parametrized to describe the effects, within the experimental domain ($E_1 = 0.015$ MeV, $E_2 = 0.96$ MeV), of all levels lying outside of the domain. If the actual discrete levels for all energies are replaced by a continuous density of reduced width, i.e., a strength function $s_{lJ}(E)$, then a smoothed real R function can be defined,[13]

$$\bar{R}_{lJ}(E) = P \int s_{lj}(E') dE'/(E' - E) , \tag{3.7}$$

where P denotes the principal value integral. The external R function is then found by subtracting the contributions from levels within the experimental domain,

$$R^{\text{ext}}_{lJ}(E) = \bar{R}_{lJ}(E) - \int \bar{s}_{lJ}(E') dE'/(E' - E) . \tag{3.8}$$

This formulation provides a good description of the effects of levels just outside the experimental domain, provided that the strength function is reasonably chosen. We parametrize[14,15] $\bar{s}_{lJ}(E)$ and $\bar{R}_{lJ}(E)$ in the domain $[E_1, E_2]$ by

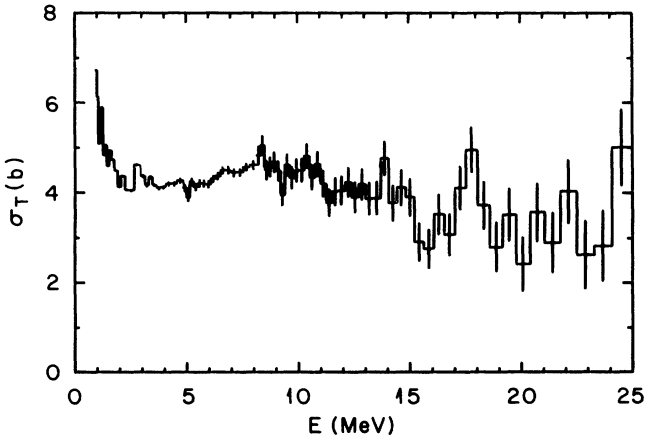

FIG. 3. Average neutron total cross sections for $n + {}^{86}\text{Kr}$ from 1 to 25 MeV. The cross sections have been averaged over suitable energy intervals in order to produce a relatively smooth plot. The error bars represent the uncertainties due to counting statistics.

$$\bar{s}_{lJ}(E)=\alpha_{lJ}+\beta_{lJ}(E-\bar{E}) , \quad (3.9)$$

and

$$\bar{R}_{lJ}(E)=a_{lJ}+b_{lJ}(E-\bar{E})+c_{lJ}(E-\bar{E})^2 , \quad (3.10)$$

where $\bar{E}$ is the midpoint energy, 0.48 MeV, and the coefficients are free parameters for fitting the data. The choice of strength function follows an iterative procedure; in the final analysis it is chosen to give a good description of the observed ratio, $\langle\gamma_{lJ}^2\rangle/D_{lJ}$, i.e., the average reduced neutron width per energy interval, as we discuss in Sec. IV. The parametrization of the external R function in terms of a smooth R function and strength function provides a simple procedure for averaging of the scattering function for comparison to the optical model, as discussed in Sec. IV E.

B. Determination of multilevel parameters

With the excellent energy resolution of ORELA, the detailed energy dependence of the cross section can be used to determine the R matrix parameters and, thereby, to deduce the scattering functions. We wrote a computer code to analyze the data using the R-matrix formulation. The program includes Doppler broadening of the calculated cross section, with an effective nuclear temperature of 330° K, and experimental resolution broadening of the resulting transmission. An essential feature of the program is that it displays both partial and total cross sections on a screen for visual comparison to the experimental cross section. Thus, we are able to examine the goodness of fit and, if the fit is not good, be guided by the partial cross sections as to which parameters may be in error. In interpreting the partial cross sections, it is important to recognize that the phase shift δ_{lJ} is a continuous function which increases by π at every resonance. Therefore, for each lJ, the partial cross section in the neighborhood of every resonance passes through a minimum of zero and a maximum of $4g_J\pi/k^2$. Overlapping resonances of the same lJ have complicated shapes because of interference. These effects may not appear so pronounced for very narrow resonances which are broadened by experimental resolution; nevertheless, even such narrow resonances may be asymmetric because of interference with a nearby strong resonance of the same lJ.

These effects are illustrated in Fig. 4 for $775<E<825$ keV. In Fig. 4(a) the points represent the measured cross section, with appropriate off-resonance averaging, and the curve shows the R-matrix fit, for which the partial cross sections are shown in Fig. 4(b). The s-, p-, and d-wave partial cross sections are represented, respectively, by short-dash, solid, and long-dash curves. For s waves each resonance appears as a simple interference minimum because the potential phase shift is about $\pi/2$ at these energies. The nonresonance s-wave contribution is accurately determined by fitting at the energies of selected $p_{3/2}$ interference minima, where the $p_{3/2}$ cross section must be zero and where the contribution of other partial waves is very small. The very broad $p_{3/2}$ resonance with $E_\lambda=775.3$ keV influences the $p_{3/2}$ interference patterns throughout the energy region of the figure, as well as at lower energies. The presence of the broad $p_{3/2}$ resonances makes it possible to identify very narrow $p_{3/2}$ resonances by their interference patterns, even though their widths may be less than the resolution width. Interference of broad $p_{1/2}$ resonances is also important; the complicated structure observed near the center of the energy region of Fig. 4(a) requires the two interfering resonances shown in Fig. 4(b). The summation of these intricate partial wave patterns yields the complicated curve of total cross section.

Having determined all of the resonance energies, lJ assignments, the R^{ext} functions, and also having determined the reduced widths to good approximation, we made final small adjustments of the widths by solving Bayes' equations using a program SAMMY,[16] which is a modification of an earlier program MULTI.[17]

C. Multilevel parameters

The final R-matrix parameters are included in Tables I–III. Table I lists the resonance parameters, E_λ, l, J, $g_J\gamma_\lambda^2$, and $g_J\Gamma_{\lambda n}$. We list the product $g_J\gamma_\lambda^2$, rather than simply γ_λ^2, because only the product is determined for those resonances where the lJ assignments are uncertain, as indicated by parentheses in the columns of l and J. Tables II and III include the parameters required in Eqs. (3.9) and (3.10) in order to calculate the $R^{\text{ext}}(E)$. Using these parameters with the assumed boundary radius from Eq. (3.5), we calculated the total cross sections for $0.015<E<0.96$ MeV. The solid curves presented in Figs. 1, 2, and 4(a) represent these cross sections with the effects of resolution and Doppler broadening included.

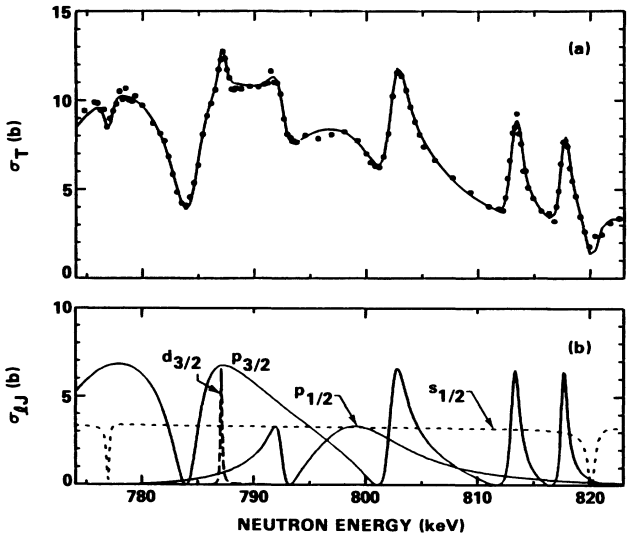

FIG. 4. An example of the complex multilevel spectrum in $n+{}^{86}$Kr. In the upper panel (a) the points represent the observed cross section and the solid line the R-matrix fit including the effects of Doppler and resolution broading. In the lower panel (b) are shown the contributions from partial waves up through $d_{3/2}$, excluding the broadening effects.

TABLE I. Resonance parameters for $^{86}Kr+n$.

E (eV)	l	J	$g\gamma^2_{\lambda n}$ (eV)	$g\Gamma_n$ (eV)	E (eV)	l	J	$g\gamma^2_{\lambda n}$ (eV)	$g\Gamma_n$ (eV)
19.238	1	$\frac{1}{2}$	1133[a]	17±2	375.15	1	$\frac{3}{2}$	8868	6340±65
27.863	(1	$\frac{3}{2}$)	741	18±2	390.30	0	$\frac{1}{2}$	781	1355±50
36.920	0	$\frac{1}{2}$	151	55±3	390.40	1	$\frac{1}{2}$	452	340±17
43.945	1	$\frac{1}{2}$	2870	130±5	392.95	2	$\frac{3}{2}$	4682	395±20
49.680	0	$\frac{1}{2}$	73	45±1	397.63	1	$\frac{3}{2}$	2048	1560±50
54.410	(1	$\frac{3}{2}$)	6512	400±8	397.63	(2	$\frac{3}{2}$)	1901	165±25
68.674	(1	$\frac{1}{2}$)	327	28±3	411.75	1	$\frac{1}{2}$	1423	1125±56
78.930	(1	$\frac{3}{2}$)	838	87±9	414.80	1	$\frac{3}{2}$	32 876	26 175±260
79.452	(1	$\frac{1}{2}$)	123	13±2	415.58	(2	$\frac{3}{2}$)	930	90±19
88.329	(2	$\frac{3}{2}$)	3616	9±2	428.96	1	$\frac{3}{2}$	616	510±25
92.189	1	$\frac{3}{2}$	4820	615±12	434.50	(2	$\frac{3}{2}$)	1320	140±20
124.67	1	$\frac{1}{2}$	1981	380±8	441.82	(2	$\frac{3}{2}$)	559	60±12
125.05	(2	$\frac{3}{2}$)	892	5±3	443.45	1	$\frac{1}{2}$	272	230±25
125.10	(1	$\frac{3}{2}$)	155	30±5	448.60	2	$\frac{3}{2}$	4953	560±28
137.50	0	$\frac{1}{2}$	3088	3180±64	454.50	1	$\frac{3}{2}$	4242	3715±80
142.21	1	$\frac{3}{2}$	2948	665±15	458.70	0	$\frac{1}{2}$	432	815±40
156.95	1	$\frac{3}{2}$	4359	1120±22	466.90	2	$\frac{3}{2}$	2824	350±17
157.80	0	$\frac{1}{2}$	1268	1400±28	481.75	(2	$\frac{3}{2}$)	373	50±12
158.13	(1	$\frac{1}{2}$)	152	40±9	485.30	1	$\frac{3}{2}$	2850	2670±50
169.60	1	$\frac{3}{2}$	2285	645±13	492.90	0	$\frac{1}{2}$	172	335±34
178.33	(1	$\frac{3}{2}$)	114	20±2	498.85	2	$\frac{3}{2}$	4896	695±25
188.89	1	$\frac{1}{2}$	4878	1575±47	504.50	1	$\frac{1}{2}$	4762	4640±120
195.60	0	$\frac{1}{2}$	311	380±19	506.51	(2	$\frac{3}{2}$)	583	85±17
206.92	0	$\frac{1}{2}$	3456	4370±44	508.10	0	$\frac{1}{2}$	1043	2065±75
211.64	1	$\frac{3}{2}$	8247	3060±60	513.16	1	$\frac{1}{2}$	158	155±17
223.30	1	$\frac{1}{2}$	4201	1660±50	515.98	1	$\frac{1}{2}$	121	120±15
224.10	1	$\frac{3}{2}$	1438	570±30	517.20	1	$\frac{3}{2}$	9318	9310±100
227.50	0	$\frac{1}{2}$	101	135±20	523.00	(1	$\frac{1}{2}$)	207	210±30
237.90	1	$\frac{3}{2}$	5459	2330±50	524.15	(1	$\frac{1}{2}$)	25	25±12
248.95	1	$\frac{3}{2}$	10 550	4750±50	526.12	2	$\frac{3}{2}$	33 432	5320±100
267.58	(2	$\frac{3}{2}$)	688	48±24	532.15	(2	$\frac{5}{2}$)	872	140±30
270.42	0	$\frac{1}{2}$	1354	1960±40	533.20	(2	$\frac{5}{2}$)	2414	395±50
270.60	1	$\frac{1}{2}$	1127	560±28	534.30	1	$\frac{3}{2}$	2169	2240±70
272.18	1	$\frac{3}{2}$	379	190±20	537.70	(1	$\frac{1}{2}$)	65	70±10
286.75	(2	$\frac{3}{2}$)	1024	35±6	539.75	0	$\frac{1}{2}$	22	45±15
293.85	1	$\frac{3}{2}$	21 782	11 880±120	540.05	1	$\frac{1}{2}$	169	175±10
307.30	(1	$\frac{3}{2}$)	117	70±11	546.00	2	$\frac{3}{2}$	879	150±22
309.70	(2	$\frac{3}{2}$)	658	40±6	547.85	2	$\frac{3}{2}$	1971	340±30
313.10	0	$\frac{1}{2}$	2066	3210±32	548.60	1	$\frac{3}{2}$	7073	7490±150
316.75	1	$\frac{3}{2}$	256	150±15	555.57	1	$\frac{1}{2}$	370	400±20
317.11	(2	$\frac{3}{2}$)	3514	185±18	558.30	1	$\frac{3}{2}$	3578	3855±70
318.30	(1	$\frac{1}{2}$)	147	88±16	567.30	1	$\frac{1}{2}$	1153	1260±50
330.30	0	$\frac{1}{2}$	856	1370±50	567.50	0	$\frac{1}{2}$	1022	2140±150
339.73	1	$\frac{1}{2}$	220	140±14	569.00	1	$\frac{3}{2}$	11 558	12 685±200
350.95	1	$\frac{3}{2}$	4474	2975±30	573.70	1	$\frac{1}{2}$	218	240±20
352.17	1	$\frac{1}{2}$	399	265±19	585.90	1	$\frac{1}{2}$	1421	1605±30

TABLE I. (*Continued*).

E (eV)	l	J	$g\gamma^2_{\lambda n}$ (eV)	$g\Gamma_n$ (eV)	E (eV)	l	J	$g\gamma^2_{\lambda n}$ (eV)	$g\Gamma_n$ (eV)
363.30	1	$\frac{3}{2}$	7877	5440±55	593.00	1	$\frac{3}{2}$	8053	9200±150
365.58	2	$\frac{3}{2}$	1381	100±10	593.25	2	$\frac{3}{2}$	1806	370±20
366.45	(0	$\frac{1}{2}$)	14	25±5	595.17	2	$\frac{3}{2}$	3730	765±40
366.80	(2	$\frac{3}{2}$)	1429	105±30	596.80	1	$\frac{3}{2}$	237	270±30
373.00	1	$\frac{1}{2}$	7899	5615±110	608.82	1	$\frac{1}{2}$	2997	3510±70
619.00	2	$\frac{3}{2}$	730	160±32	817.60	1	$\frac{3}{2}$	873	1345±270
622.98	1	$\frac{1}{2}$	1839	2200±90	820.30	0	$\frac{1}{2}$	301	760±190
624.38	0	$\frac{1}{2}$	176	385±60	825.90	(1	$\frac{1}{2}$)	35	55±16
625.00	1	$\frac{3}{2}$	55 784	67 000±1350	828.40	0	$\frac{1}{2}$	62	160±45
626.14	2	$\frac{3}{2}$	2218	505±76	829.80	(2	$\frac{3}{2}$)	593	235±40
631.35	1	$\frac{3}{2}$	445	540±80	831.10	0	$\frac{1}{2}$	56	145±43
641.20	0	$\frac{1}{2}$	525	1170±120	832.00	(2	$\frac{3}{2}$)	647	260±40
643.65	1	$\frac{3}{2}$	432	535±60	836.40	1	$\frac{3}{2}$	12 548	19 700±1000
645.55	1	$\frac{1}{2}$	5177	6415±60	843.00	(2	$\frac{3}{2}$)	9268	3790±380
648.04	(2	$\frac{5}{2}$)	661	160±40	842.80	1	$\frac{3}{2}$	5955	9410±1410
657.20	1	$\frac{1}{2}$	1087	1370±85	851.00	0	$\frac{1}{2}$	126	325±97
665.30	1	$\frac{3}{2}$	19 285	24 585±740	852.50	1	$\frac{3}{2}$	955	1525±380
670.50	1	$\frac{3}{2}$	33 016	42 395±850	852.80	(2	$\frac{3}{2}$)	441	185±56
680.00	0	$\frac{1}{2}$	83	190±15	860.05	(1	*cf* 12)	618	995±300
680.70	2	$\frac{3}{2}$	901	245±73	861.55	(1	$\frac{1}{2}$)	898	1450±180
684.50	1	$\frac{3}{2}$	32 645	42 735±850	866.78	1	$\frac{3}{2}$	2334	3780±570
686.25	(2	$\frac{3}{2}$)	870	240±72	868.50	(2	$\frac{3}{2}$)	607	260±60
694.25	(2	$\frac{3}{2}$)	850	240±72	871.80	1	$\frac{3}{2}$	7006	11 405±900
695.20	0	$\frac{1}{2}$	258	600±80	874.00	0	$\frac{1}{2}$	37	98±20
700.60	1	$\frac{1}{2}$	636	850±100	875.00	(2	$\frac{5}{2}$)	4523	1985±200
701.20	1	$\frac{3}{2}$	8226	11 015±330	877.75	(2	$\frac{3}{2}$)	491	215±22
707.00	1	$\frac{1}{2}$	10 140	13 680±550	880.00	1	$\frac{1}{2}$	1769	2905±435
710.50	1	$\frac{3}{2}$	3240	4390±440	880.25	(2	$\frac{3}{2}$)	452	200±60
718.80	2	$\frac{3}{2}$	1212	365±90	885.05	1	$\frac{3}{2}$	3183	5250±525
718.25	1	$\frac{1}{2}$	425	580±87	887.85	1	$\frac{3}{2}$	520	860±70
721.80	2	$\frac{3}{2}$	1049	320±32	889.25	(0	$\frac{1}{2}$)	32	85±42
726.00	1	$\frac{3}{2}$	4920	6800±68	891.30	1	$\frac{3}{2}$	657	1090±110
726.42	(2	$\frac{5}{2}$)	1208	370±37	893.70	1	$\frac{1}{2}$	1133	1885±190
728.80	0	$\frac{1}{2}$	1188	2820±500	898.00	(2	$\frac{5}{2}$)	4440	2045±510
730.40	2	$\frac{3}{2}$	3832	1190±83	902.50	(2	$\frac{3}{2}$)	946	440±70
732.50	1	$\frac{3}{2}$	9398	13 095±850	903.00	1	$\frac{3}{2}$	34 073	57 190±3900
734.30	1	$\frac{1}{2}$	5021	7015±490	905.30	(2	$\frac{5}{2}$)	1334	625±180
736.20	2	$\frac{5}{2}$	478	150±10	908.60	(2	$\frac{3}{2}$)	476	225±78
741.00	1	$\frac{3}{2}$	1951	2750±82	910.30	(1	$\frac{1}{2}$)	138	235±70
745.20	0	$\frac{1}{2}$	360	865±180	913.63	(2	$\frac{3}{2}$)	1097	520±78
748.50	1	$\frac{3}{2}$	8267	11 750±1200	914.94	(2	$\frac{3}{2}$)	2641	1260±126
749.50	1	$\frac{1}{2}$	4570	6505±780	918.80	(2	$\frac{5}{2}$)	1409	675±170
752.46	(2	$\frac{3}{2}$)	1462	480±48	923.60	1	$\frac{1}{2}$	270	465±115
755.00	0	$\frac{1}{2}$	736	1780±375	923.65	1	$\frac{3}{2}$	2255	3860±770
760.00	1	$\frac{1}{2}$	3507	5055±650	924.60	(2	$\frac{3}{2}$)	1217	591±160
761.20	1	$\frac{3}{2}$	10 124	14 610±1320	929.00	0	$\frac{1}{2}$	867	2322±550

TABLE I. (*Continued*).

E (eV)	l	J	$g\gamma^2_{\lambda n}$ (eV)	$g\Gamma_n$ (eV)	E (eV)	l	J	$g\gamma^2_{\lambda n}$ (eV)	$g\Gamma_n$ (eV)
775.30	1	$\frac{3}{2}$	20 962	30 755±2500	932.30	(2	$\frac{5}{2}$)	1125	554±160
777.00	0	$\frac{1}{2}$	107	265±80	934.20	(2	$\frac{3}{2}$)	1025	507±160
786.00	1	$\frac{3}{2}$	7284	10 820±650	934.75	1	$\frac{3}{2}$	4604	7961±900
787.20	(2	$\frac{3}{2}$)	903	325±5	938.85	(2	$\frac{3}{2}$)	1907	952±280
791.50	1	$\frac{1}{2}$	2381	3560±35	939.90	1	$\frac{3}{2}$	3536	6144±1200
797.30	1	$\frac{1}{2}$	6561	9870±98	942.00	1	$\frac{1}{2}$	7878	13 714±2000
802.50	1	$\frac{3}{2}$	2246	3400±50	941.00	(2	$\frac{3}{2}$)	795	398±120
813.20	1	$\frac{3}{2}$	1242	1905±34	946.50	(2	$\frac{3}{2}$)	1020	517±150

[a]All values of $g\gamma^2_{\lambda n}$ and $g\Gamma_n$ calculated for the R-matrix channel radius $a_c = 6.4$ fm.

We emphasize that the partial cross sections, and the corresponding phase shifts and scattering functions, have been determined with little ambiguity for the $s_{1/2}$, $p_{1/2}$, and $p_{3/2}$ partial waves.

Also listed in Table I are the products $g_J\Gamma_{\lambda n}$:

$$g_J\Gamma_{\lambda n} = 2P_l(E_\lambda)g_J\gamma^2_{\lambda n} \ . \tag{3.11}$$

This quantity is often referred to as the observed width of the resonance at $E_{\lambda n}$. Actually, $\Gamma_{\lambda n}$ may be quite different from the observed width if there is strong interference with nearby levels. For example, the $\frac{3}{2}^-$ resonance with $E_\lambda = 789$ keV has $\Gamma_{\lambda n} = 5.41$ keV but, as shown in Fig. 4(a), this "width" is not easily identified with an observed feature in the complicated multilevel structure. Even in the absence of resonance-resonance interference, the quantity $\Gamma_{\lambda n}$ may not be independent of the assumed boundary radius. Another consequence of multilevel interference is that the "observed" resonance energy may differ somewhat from E_λ, even though the boundary condition has been set equal to the shift factor, and that E_λ also depends on the assumed boundary radius. Even so, the scattering functions are well determined and are not functions of the boundary conditions.

IV. AVERAGE PROPERTIES

The average properties of interest from the R-matrix analysis are the level spacings, the strength functions, and the R^{ext} functions. The interest is related to statistical and optical models.

A. Level spacings

An accurate measurement of the level spacings for each J^π is difficult because the levels with widths smaller than the experimental resolution width may not be observed and, even if observed, may be assigned an incorrect J^π in the subsequent analysis. In the present case, however, the excellent energy resolution and small backgrounds for ORELA, and the relatively large level spacings apparent from Figs. 1 and 2 are such that few missed or spuriously included resonances are expected for the $J^\pi = \frac{1}{2}^+$, $\frac{1}{2}^-$, and $\frac{3}{2}^-$ resonances. Therefore, the following corrections to the observed level spacings have little uncertainty.

To correct for the missing levels we assume that the observed reduced widths are drawn from Porter-Thomas (PT) distributions and that no resonances are missed with $\gamma^2_{\lambda n}$ greater than $\langle\gamma^2_{\lambda n}\rangle/4$. To perform this test[18] one forms a subset of resonances with given J^π, beginning with the largest $\gamma^2_{\lambda n}$, and successively includes the next smaller reduced width until the ratio of $\langle\gamma^2_{\lambda n}\rangle$ to $\langle(\gamma^2_{\lambda n})^{1/2}\rangle$ is the result expected for a sample obtained by drawing widths larger than $\frac{1}{4}$ the distribution mean from a PT distribution. The results of this test for the $s_{1/2}$, $p_{1/2}$, and $p_{3/2}$ resonances are shown in Fig. 5, where the

TABLE II. Average parameters for $n + {}^{86}$Kr.

J^π	N^{obs}	N^m	D_{lj} (keV)	$\bar{s}_{lJ}$ α_{lJ}	β_{lJ} (MeV^{-1})	Δ_3^{obs}
$\frac{1}{2}^+$	32	3[a]	26.2(21)[a]	0.022(6)		0.3[b]
$\frac{1}{2}^-$	47	3	18.8(14)	0.094(20)	0.155	0.6
$\frac{3}{2}^-$	62	4	14.0(10)	0.27(5)	0.51	0.4
$l=2$	59		14.8	0.024[c]		

[a]Estimated number of missed levels, N^m, used in calculation of D_{lJ}. The numbers in parentheses are the uncertainty estimates, e.g., 26.2(21)=26.2±2.1.

[b]See text for energy subintervals for which Δ_3 was calculated. The expected Δ_3 is 0.3(1) in every case.

[c]The best estimate for the d-wave strength function is $\bar{s} = \sum_\lambda g_J\gamma^2_\lambda/(5N^{\text{obs}}D_{lJ})$.

TABLE III. Parameters of the smooth R function, $\bar{R}$.

J^π	$\bar{R}$ a	b (MeV^{-1})	c (MeV^{-2})	$\Delta\bar{R}$ [a]
$\frac{1}{2}^+$	−0.16	0.07		0.02
$\frac{1}{2}^-$	0.65	0.1		0.2
$\frac{3}{2}^-$	0.95	−0.42	−2.1	0.05
$\frac{3}{2}^+$	0.0			0.2

[a]Uncertainty in $\bar{R}$ at the midpoint of the region $[E_1,E_2]$.

histograms are the observed distributions and the solid curves are from the PT distributions deduced from the above test in which the histograms are fit for

$$x \equiv (\gamma_\lambda^2)^{1/2} > (\langle \gamma_\lambda^2 \rangle)^{1/2}/2 \ . \tag{4.1}$$

From the extrapolation of the solid curves to $x=0$ we find $N^m=3$, 3, and 4 missed resonances for the $\frac{1}{2}^+$, $\frac{1}{2}^-$, and $\frac{3}{2}^-$ data sets, respectively. The dashed curves are the expected distribution assuming no missed resonances. Thus, even for the smallest data set ($s_{1/2}$), fewer than 10% of the resonances expected in the 0.015 to 0.96 MeV energy range appear to have been missed. The histograms in Fig. 6 represent the cumulative number of levels versus energy for the $s_{1/2}$, $p_{1/2}$, and $p_{3/2}$ partial waves. We have corrected for missing levels by including, for each histogram, N^m levels selected arbitrarily from the resonances in Table I with unassigned J^π.

Table II includes the number $N^{\rm obs}$ of observed resonances, the number N^m of missed levels, and the average level spacings defined by the equation

$$D_{lJ} \equiv (E_2-E_1)/(N^{\rm obs}+N^m-1) \ . \tag{4.2}$$

These average spacings are consistent with those reported[4] for other nuclei in this mass region.

Actually, it is clear from the slopes of the histograms in Fig. 6 that the level spacings decrease with increasing energy. These three data sets are among the most nearly complete sets of resonances of known J^π available over a sufficiently large energy region that the expected energy dependence in level density models can be studied. In describing nuclear level densities, most works[3,19–24] have concentrated on the backshifted Fermi-gas model for which the excitation energy U is measured from a fictive ground-state energy U_0,

$$U = E + (S_n - U_0) \ , \tag{4.3}$$

where S_n is the neutron separation energy, i.e., 5.2 MeV for $n + {}^{86}$Kr. The total density summed over J is

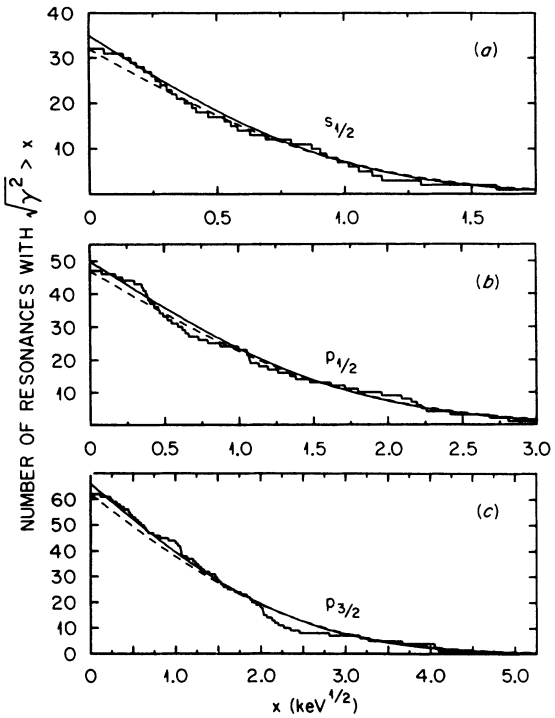

FIG. 5. Porter-Thomas test for missing resonances. The histograms represent the number of $s_{1/2}$, $p_{1/2}$, and $p_{3/2}$ resonances in $n + {}^{86}$Kr with $(\gamma_\lambda^2)^{1/2}$ greater than the abscissa. The dashed curves correspond to results expected if widths are drawn from Proter-Thomas distributions assuming no missed levels. The solid curves are for 3, 3, and 4 missed resonances for $s_{1/2}$, $p_{1/2}$, and $p_{3/2}$, respectively.

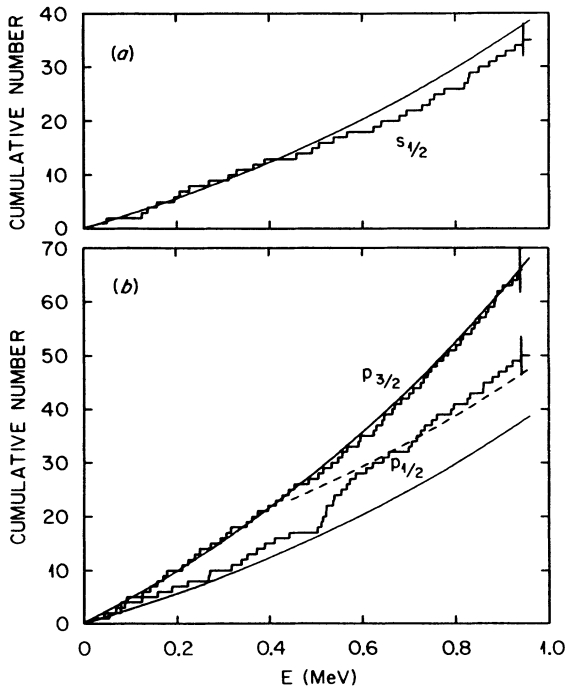

FIG. 6. The cumulative number of observed levels vs neutron energy for each partial wave, $s_{1/2}$, $p_{1/2}$, and $p_{3/2}$. The curves are calculated using the backshifted Fermi-gas model for the nuclear level density. The level density parameters $a=8.5$ MeV^{-1} and $U_0=0.25$ MeV were determined by fitting the total number of $p_{3/2}$ resonances from 18 to 1000 keV and the low-lying excited levels in ^{87}Kr from 1.5 to 2.5 MeV above the ground state. The dashed curve in (b) is obtained by adding eight resonances to the solid curve for $p_{1/2}$.

$$\rho_{\rm tot}(U)=(12\sqrt{2\sigma})^{-1}a^{-1/4}U^{-5/4}\exp[-2\sqrt{(aU)}]\ , \quad (4.4)$$

and the density for a given J is

$$\rho_J(U)=(2\sigma^2)^{-1}\rho_{\rm tot}(U)(2J+1) \times\exp[-(J+\tfrac{1}{2})^2/2\sigma^2]\ . \quad (4.5)$$

The energy dependence of the spin cut-off factor σ^2 is modeled[24] as

$$\sigma^2=0.0888\sqrt{(aU)}A^{1/3}\ , \quad (4.6)$$

where A is the nuclear mass number. The two parameters a and U_0 can be adjusted to fit the observed number of levels in two selected regions of excitation, one above and the other below S_n. For the bound region we use the total number $N^{\rm ex}$ of low-lying states reported by Raman *et al.*[3] for excitation energies between 1.5 and 2.5 MeV. For the unbound region we could take the total number of levels $N(J^\pi)$, corrected for missed levels, from any one of the three distributions in Figs. 5 or 6; we choose $N(\frac{3}{2}^-)$ because the uncertainty due to missed levels is the least for $J^\pi=\frac{3}{2}^-$. Thus, the parameters a and U_0 are adjusted to satisfy the two equations,

$$N^{\rm ex}=\int dU\,\rho_{\rm tot}(U)=16\ , \quad (4.7)$$

and

$$N(\tfrac{3}{2}^-)=\tfrac{1}{2}\int dU\,\rho_{3/2}(U)=65\ , \quad (4.8)$$

where the integrations are over the experimental domains described above. The factor $\frac{1}{2}$ in Eq. (4.8) is a result of the assumption that both parities for a given J are equally represented. We find $a=8.5$ MeV^{-1} and $U_0=0.25$ MeV; the solid curves in Fig. 6 represent the resulting calculated cumulative number of levels for $J^\pi=\frac{1}{2}^+$, $\frac{1}{2}^-$, and $\frac{3}{2}^-$.

We emphasize that, since the parameters of our model have been chosen to fit the $p_{3/2}$ histogram, the curves for $s_{1/2}$ and $p_{1/2}$ are predictions. The quality of the prediction for each curve can be judged by comparison to the error bar, which represents the uncertainty expected for a Wigner distribution of levels spacings. We see that the prediction is good for $s_{1/2}$; however, for $p_{1/2}$ there is an excess number of resonances in the region from 500 to 600 keV which produces a step in the cumulative number of observed resonances which is not described by this model. One possible explanation of this failure of the model could be that the model J dependence is incorrect. On the other hand, the failure could result from an unusual nonstatistical behavior in this energy region. In fact, in the following paragraph we show that the distribution is nonstatistical. If we assume that to be the case and add eight resonances to $N(\frac{1}{2}^-)$ at 600 keV we find the cumulative number of resonances represented by the dashed curve in Fig. 6(b), where the level density above the step is calculated using the same level density parameters as for the solid curve below 500 keV.

The above statistical analysis based on the PT distribution gave no hint of an unusual behavior in the 500–600 keV region because that test is insensitive to the resonance spacings; however, the Dyson-Mehta[25] Δ_3 statistic is sensitive to the spacings. For this test one assumes that the levels of a given J^π are drawn from a population (Wigner distribution) of level spacings with constant mean. Since the level density varies with energy, we divide the region 0 to 960 keV into three subintervals and apply the Δ_3 test to each subinterval, namely, 0–300, 300–600, and 600–960 keV. The resulting average Δ_3 statistics are given in Table II. For $J^\pi=\frac{1}{2}^+$ and $\frac{3}{2}^-$ they are consistent with the results expected if few resonances are missed or spuriously included in those data sets. For $J^\pi=\frac{1}{2}^-$, however, the value of $\Delta_3=0.6$ is twice the expected value, $\Delta_3=0.3\pm0.1$; this is a consequence of the unusual density in the region from 500 to 600 keV. In fact, any subinterval including the 11 resonances between 500 and 600 keV results in values of Δ_3 approximately four times the expected value. We have carefully studied the R-matrix fits in this region and conclude that the two resonances at 523 and 524 keV might be other than $\frac{1}{2}^-$; but, if so, they must have $J>\frac{3}{2}$ because those two do not show interference with the nearby broad $\frac{3}{2}^+$ resonances. The assignments for these two resonances are marked as uncertain in Table I but are included as $\frac{1}{2}^-$ in the following discussion since removing either or both does not improve the Δ_3 statistic. The possibility of a doorway[26] in the $p_{1/2}$ channel near 550 keV will be discussed in Sec. V.

With the exception of the unusual "step" in the $p_{1/2}$ cumulative number of levels, the backshifted Fermi-gas model is seen to give an excellent description of all three data sets. The values for the parameters a and U_0 found here are consistent with systematic trends[21–24] in this mass region. The present value of a is significantly smaller than the value 9.7 MeV^{-1} found by Raman *et al.*[3] based on their measurements and analysis over a smaller neutron energy range, $0<E<0.4$ MeV.

B. Strength functions

The strength functions $\bar{s}_{lJ}$ are the slopes of the cumulative reduced width versus energy distribution shown in Fig. 7 for s-, p-, and d-wave resonances. We have not corrected these strength functions for missing levels since our estimate of the effect of missing a few small resonances is less than 1% of the observed strength. We present in Table II for $J^\pi=\frac{1}{2}^+$, $\frac{1}{2}^-$, $\frac{3}{2}^-$ and for $l=2$ the strength function parameters α_{lJ} and β_{lJ} [see Eq. (3.9)]. We note that for s waves a constant strength is an adequate description of the data while for the the p waves an energy dependence is required. The increase, $\beta_{lJ}>0$, in the p-wave strength functions is expected if the $3p$ single-particle state is just unbound at mass 87. In fact, the $3p$ state is bound near mass 95, i.e., where the p-wave size resonance has its maximum.[4] Qualitatively, the effect of the spin-orbit interaction is to move the $3p_{3/2}$ size resonance downward in mass toward ^{86}Kr and the $3p_{1/2}$ resonance upward away from ^{86}Kr. Thereby, the $p_{3/2}$ strength function is increased relative to that for $p_{1/2}$. As discussed in Ref. 7, the observed difference in strength apparent from Fig. 7(b) is about 50% larger than predicted from a model with a standard spin-orbit term.

In Fig. 7(c) the histogram labeled d is the quantity $g\gamma_\lambda^2/(2l+1)$ summed over $l=2$ resonances, except for the broad $d_{3/2}$ resonance at 526 keV. In other words, the sum extends over all resonances which have definite $l=2$ assignments but which could be assigned either $d_{3/2}$ or $d_{5/2}$. The curve represents a linear approximation to the histogram and the slope of this curve is an estimate of the d-wave strength function. Since there are no definitive assignments with $J=\frac{5}{2}$, this slope provides the best estimate for the $d_{5/2}$ strength function. It would also provide the best estimate for $d_{3/2}$ if the broad $d_{3/2}$ resonance at 526 keV had not been in the range of this measurement. The histogram labeled $d_{3/2}$ in Fig. 7(c) includes the $d_{3/2}$ resonance at 526 keV. The line is a linear fit to the histogram, and the slope of this line is an estimate of the $d_{3/2}$ strength function. Clearly, the reduced width of this single resonance is unusually large; it corresponds to about 2% of the Wigner limit. The probability of drawing a level of such large width from a PT distribution is less than 0.05%. We made many attempts to fit this observed resonance pattern by replacing the $d_{3/2}$ level by other combinations of levels and assignment; however, we found it impossible to fit in this region with any other assignment. In Sec. V this resonance is discussed as evidence for a doorway[26] state in the $d_{3/2}$ channel.

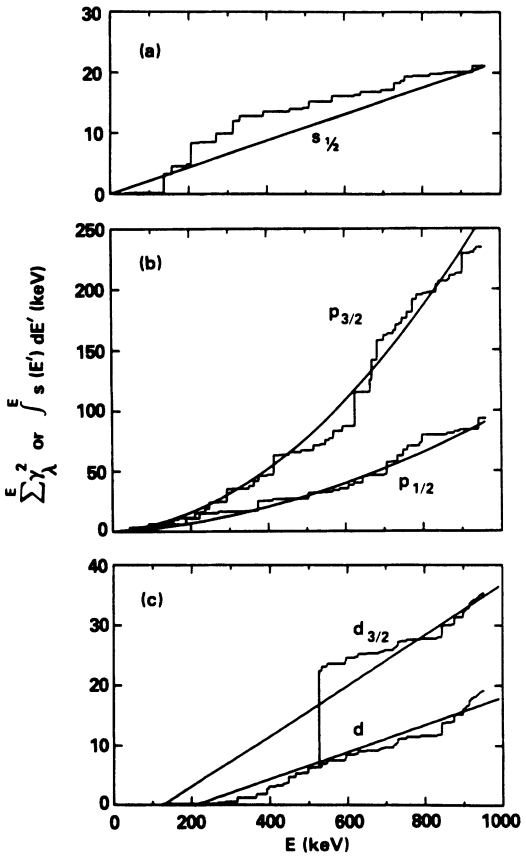

FIG. 7. Cumulative reduced widths for s- and p-wave resonances. The histograms show the summation of observed reduced widths and the smooth curves are least-squares fits of the integral of the strength function, Eq. (3.9), to the cumulative reduced width. The parameters α_{lJ} and β_{lJ} are listed in Table II.

C. Conventional definition of the strength function

In reporting strength functions it has been conventional to report[4] a quantity, $\langle\Gamma_n^{lJ}\rangle/D_{lJ}$, which is proportional to the product of the boundary radius and the strength function,

$$\langle\Gamma_n^{lJ}\rangle/D_{lJ}=(4.39\times10^{-4})(A/A+1)a_c\tilde{s}_{lJ}\ . \tag{4.9}$$

For s-wave neutrons at low energies this definition has the virtue of being independent of the boundary radius. In general, even for s waves, that invariance does not hold[27] at energies of a few hundred keV; however, it does hold approximately in the present case. Furthermore, it is reasonable to assume the s-wave strength function to be independent of energy for $n+{}^{86}$Kr. Hence, for s waves we find the conventional strength function,

$$S_0=\langle\Gamma_n^0\rangle/D_0=(0.61\pm0.17)\times10^{-4},\quad 0<E<1\ \text{MeV}\ . \tag{4.10}$$

This result agrees with the estimate by Raman *et al.*,[3] $(0.9\pm0.4)\times10^{-4}$.

For p waves, the invariance with respect to a_c does not hold at any energy, except perhaps by accident. At very low energies, for example, the imaginary part of the p-wave scattering function is a definite quantity and is expressible as

$$\mathrm{Im}\langle S_{lJ}\rangle=2\pi k^3 a_c^3\tilde{s}_{lJ}\ , \tag{4.11}$$

leading to the conclusion that the invariant quantity for $l=1$ at low energies is $(a_c^3\tilde{s}_{lJ})$, not $(a_c\tilde{s}_{lJ})$. At higher energies the dependence on the boundary radius is different. Thus the "observed" energy dependence in $\tilde{s}_{lJ}(E)$ depends in part on the chosen boundary radius. For ^{86}Kr the optical model analysis presented in Ref. 7 makes clear that the observed $\tilde{s}_{lJ}(E)$ increases too rapidly with energy to be describe by an optical model with any reasonable boundary condition. This is discussed in Ref. 7 as evidence for a doorway in the $\frac{3}{2}^-$ scattering channel.

D. $\bar{R}$ and R^{ext} functions

The solid curves in Fig. 8 represent the external R functions $R^{\text{ext}}(E)$ which are calculated from Eq. (3.8) for the $s_{1/2}$, $p_{1/2}$, $p_{3/2}$, and $d_{3/2}$ partial waves using the parameters listed in Tables II and III. Those parameters were deduced primarily from the observed interference patterns for a few broad resonances for each partial wave. Reliable parameters are found in this manner even if only one or two large resonances exist in the region of analysis, as in the case of the $d_{3/2}$ resonances at 525 and 834 keV. The uncertainties in R^{ext}, which are represented by the vertical bars in Fig. 8, have been estimated from the change in resonance asymmetry and/or off-resonance cross section resulting from small changes in the assumed parameters. Shown in Fig. 8 as dashed curves are the smooth functions $\bar{R}_{lJ}(E)$. For p waves the

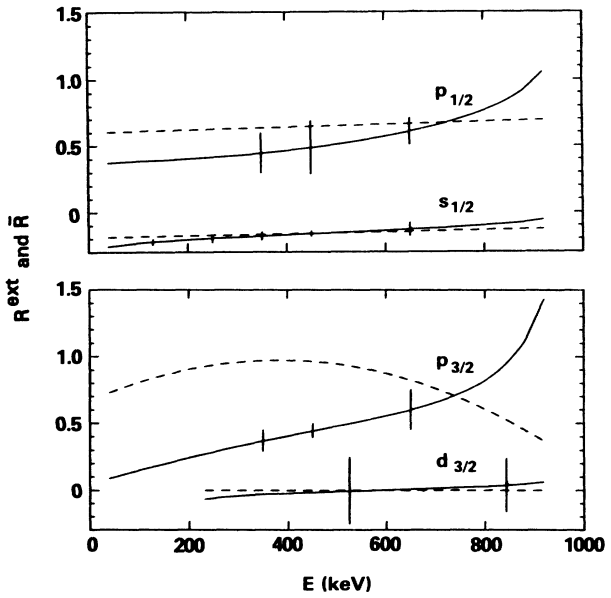

FIG. 8. Empirical external R functions R^{ext} (solid curves), deduced from the R-matrix analysis, and the corresponding smoothed R functions $\bar{R}$ (dashed curves). The curves represent Eqs. (3.8) and (3.10) and the parameters a_{lJ}, b_{lJ}, and c_{lJ} are listed in Table III. Representative error bars for R^{ext} are shown at selected energies.

energy dependences of these functions are correlated with that for the parametrization of the strength functions $\bar{s}_{lJ}(E)$; however, for s waves, there is little uncertainty in $\bar{R}$.

The s-wave potential scattering radius R' is determined from the $\bar{R}$ function evaluated at $E=0$,

$$R'=a_c[1-\bar{R}_{s1/2}(0)]=7.62 \text{ fm} , \tag{4.12}$$

and is independent of the choice of the boundary radius a_c. This value of R' agrees well with the values reported[4] for other nuclei in this mass region.

E. Average scattering functions

The primary interest in the function $\bar{R}(E)$ and in the strength function $\bar{s}_{lJ}(E)$ is related to the average scattering function $\langle S_{lJ}(E)\rangle$ because $\langle S_{lJ}(E)\rangle$ can be calculated to a good approximation[13–15] from a simple expression in $\bar{R}(E)$ and $\bar{s}_{lJ}(E)$:

$$\langle S_{lJ}(E)\rangle = e^{2i\varphi_l(E)}\frac{[1+iP_l(E)\mathbf{R}_{lJ}(E)]}{[1-iP_l(E)\mathbf{R}_{lJ}(E)]} , \tag{4.13}$$

where

$$\mathbf{R}_{lJ}(E)=\bar{R}_{lJ}(E)+i\pi\bar{s}_{lJ}(E) . \tag{4.14}$$

Qualitatively, the empirical functions $\bar{R}(E)$ and $\bar{s}_{lJ}(E)$ play parallel roles in determining the average scattering function; both are needed to determine both the real and imaginary parts of $\langle S_{lJ}(E)\rangle$. In like manner, both are needed if one wishes to interpret $\langle S_{lJ}(E)\rangle$ in terms of a mean field, i.e., an optical-model potential. Often the strength function, which comes from the average resonance parameters, is closely related to the imaginary part of the mean field whereas the $\bar{R}$ function, which comes from the nonresonance scattering, is more closely related to the real part of the field. Further discussions relating these empirical functions to the mean field of ^{86}Kr are the subject of Ref. 7.

V. DOORWAYS

An unusually large concentration of reduced width in a relatively narrow energy interval is often associated with doorway[26] structure. In fact, concentrations of reduced width are observed in Fig. 7 for $s_{1/2}$ ($E\approx 0.125$ MeV), $p_{1/2}$ ($E\approx 0.7$ MeV), $p_{3/2}$ ($E\approx 0.6$ MeV), and $d_{3/2}$ ($E\approx 0.525$ MeV). In the case of the $p_{3/2}$, the concentration of reduced widths near $E=0.6$ MeV tends to be obscured in the figure by the smooth curve. However, this curve is empirical; it is based on a strength function [Eq. (3.9) and Table II] with a large energy coefficient which is inconsistent with an optical-model description.[7] The more reasonable strength function calculated[7] from an optical model increases much more slowly with energy and is consistent with the observed strengths both above and below the "doorway." The most likely $\frac{3}{2}^-$ doorway would arise from the $1g_{7/2}\times 3^-$ particle vibration. The deformation parameter for the 3^- state at 3.10 MeV in ^{86}Kr is quite large,[28] 0.142. Coupling with the large $g_{7/2}$ fragment[29] at -3.00 MeV in ^{87}Kr would produce a doorway, in first approximation, near 0.1 MeV. A $\frac{1}{2}^-$ doorway would also be expected from the $1g_{7/2}\times 3^-$ particle vibration; however, there is only a small concentration of $p_{1/2}$ reduced widths observed near $E=0.7$ MeV. On the other hand, in Fig. 6 there is observed an unusually high density of $p_{1/2}$ levels near $E=0.55$ MeV. However, in this case the resonances are very narrow. In fact, the average reduced width of the eight smallest of the eleven observed $p_{1/2}$ resonances between 0.5 and 0.6 MeV is less than 10% of that for the full energy region.

The small reduced widths in the possible p-wave doorways can be understood to result from the fact that the p-wave radial wave functions for $E\approx 0.6$ MeV neutrons have nodes near the nuclear surface. In Fig. 9 the curves represent the s-, p-, and d-wave radial functions calculated at $E=0.6$ MeV for the real part of the optical-model potential which is developed in Ref. 7. There are two curves each for p- and d-wave neutrons as a consequence of the spin-orbit interaction. The vertical line is drawn at the radius of the real Woods-Saxon potential. Since the $p_{1/2}$ function has a surface node, the reduced width for a $p_{1/2}$ doorway is expected to be small because the particle-vibration coupling is concentrated near the surface. For the same reason, the $p_{3/2}$ doorway would be expected to have somewhat larger, but still small, reduced widths. This significance of the position of the radial node was pointed out by Horen *et al.*[30] in connection with a coupled-channel analysis of the $n+{}^{208}$Pb reaction. The appearance of narrow, closely spaced resonances due to a weak residual interaction is similar to the fine structure reported[31,32] in isobaric analogue states excited in (p,p) reactions. In the case of isobaric analogue states it

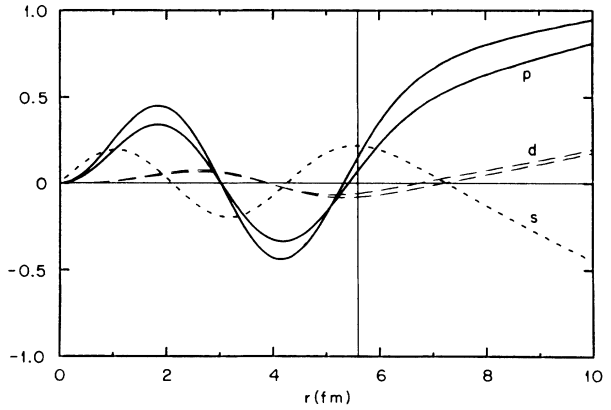

FIG. 9. The radial wave functions for p waves (solid), s waves (short-dashed) and d waves (long-dashed) calculated at 0.55 MeV for the real part of the optical potential developed in the Ref. 7. The figure demonstrates that the p-wave functions have nodes, whereas the s- and d-waves have antinodes, near the nuclear radius, which is represented by the vertical line.

is the weak coulomb interaction which is responsible for the large number of observable levels with small widths.[31]

As shown in Fig. 9, the s- and d-wave radial wave functions have antinodes in the vicinity of the nuclear surface. Hence particle-core interactions would be expected to produce relatively large reduced widths in the doorways. Both $\frac{1}{2}^+$ and $\frac{3}{2}^+$ doorways could be formed near 0.3 MeV by coupling the $1g_{7/2}$ single-particle fragment with the 4^+ state reported[28] at 3.33 MeV. In the case of $s_{1/2}$ the strength function near 0.125 MeV is more than twice that above 0.4 MeV. In Fig. 7(c) for d waves the increased reduced width at 0.526 MeV is concentrated in a single resonance rather than distributed over several resonances. This suggests that the interaction is so strong that the spreading of the underlying levels exceeds their spacings such that their amplitudes add to give a "single" resonance. It is reasonable to expect a corresponding increase in the $d_{5/2}$ channel, but none is observed in Fig. 7(c). An alternative interpretation is that the isolated $d_{3/2}$ resonance is a fragment of the single-particle $2d_{3/2}$ state, which is concentrated mostly at about -2.5 MeV.[28] The resonance has about 2% of the single-particle width.

VI. CONCLUSIONS

The neutron transmission measurement reported here provides the total neutron cross section from 15 keV to 25 MeV. For these data, R-matrix analysis provides strength functions, external R functions, and level densities just above neutron binding in the $n + {}^{86}\mathrm{Kr}$ system. The reduced widths γ_λ^2 and the external R function $R_{lJ}^{\mathrm{ext}}(E)$ provide a precise description of the scattering functions $S_{lJ}(E)$ for the $s_{1/2}$, $p_{1/2}$, and $p_{3/2}$ scattering channels. The scattering functions for $p_{1/2}$ and $p_{3/2}$ show the effects of the spin-orbit potential and also the effects of the $3p$ single-particle orbit, which is just unbound for nuclei in this mass region. In Ref. 7 the average scattering functions $\langle S_{lJ}(E) \rangle$ are found to be well described by an optical model which is based not only on analyses of scattering data at energies of several MeV but also on the known level structure of the bound states in ${}^{87}\mathrm{Kr}$.

Statistical arguments show that very few $s_{1/2}$, $p_{1/2}$, and $p_{3/2}$ resonances have been missed in the high-resolution experiment or misassigned in the subsequent R-matrix analysis. Therefore, the observed level densities in these three channels make a detailed analysis possible in terms of the backshifted Fermi-gas model.

Evidence is found for possible doorway states near $E = 0.55$ and 0.65 MeV for the $p_{1/2}$ and $p_{3/2}$ scattering channels, respectively. However, these two structures exhibit very different characteristics. The $p_{3/2}$ structure has the familiar doorway character of a concentration of reduced width; however, the $p_{1/2}$ structure is a local concentration of levels with quite small reduced widths. This difference in character is interpreted in terms of the difference in radius of the nodes in the radial wave functions for the two partial waves.

ACKNOWLEDGMENTS

We are grateful for helpful discussions with Dr. P. Fu, Dr. D. Horen, Dr. N. Larson, Dr. M. McEllistrem, and Dr. S. Raman about various aspects of the analysis. We are also grateful to the ORELA operators, who maintained the operating conditions for these measurements during a time when a number of accelerator modifications were being made, and to J. G. Craven, whose help was essential for the computer analysis of the large amount of data.

[1] A. V. Ignatyuk, Report Trans. IAEA, INDC(CCP)-233/L (1985).

[2] P. G. Young, in *Proceedings of the International Conference on Nuclear Data for Science and Technology, Antwerp, Belgium, 1982,* edited by K. H. Böckhoff (Reidel, Dordrecht, 1983), p. 506.

[3] S. Raman, B. Fogelberg, J. A. Harvey, R. L. Macklin, and P. H. Stelson, Phys. Rev. C **28**, 602 (1983).

[4] S. F. Mughabghab, *Neutron Cross Sections* (Academic, New York, 1984) Vol. 1.

[5] Zo in OK, V. G. Nikolenko, A. B. Popov, and G. S. Samosvat, Pis'ma Zh. Eksp. Teor. Fiz. **38**, 304 (1983) [JETP Lett. **38**, 363 (1983)].

[6] C. Mahaux and H. Ngô, Nucl. Phys. **A378**, 205 (1982).

[7] C. H. Johnson, R. F. Carlton and R. R. Winters, to be submitted to Phys. Rev. C.

[8] D. C. Larson, N. M. Larson, and J. A. Harvey, Oak Ridge National Laboratory Report ORNL/TM-8880 (unpublished).

[9]D. C. Larson, N. M. Larson, J. A. Harvey, N. W. Hill, and C. H. Johnson, Oak Ridge National Laboratory Report, ORNL/TM-8203 and Report ENDF-333 (unpublished).
[10]J. A. Harvey and N. W. Hill, Nucl. Instrum. Methods **162**, 507 (1979).
[11]C. M. Perey, J. A. Harvey, R. L. Macklin, F. G. Perey, and R. R. Winters, Phys. Rev. C **27**, 2556 (1983).
[12]A. Smith, P. Guenther, D. Smith, and J. Whalen, Nucl. Sci. Eng. **72**, 293 (1979).
[13]A. M. Lane and R. G. Thomas, Rev. Mod. Phys. **30**, 257 (1958).
[14]C. H. Johnson, C. Mahaux and R. R. Winters, Phys. Rev. C **32**, 359 (1985).
[15]C. H. Johnson and R. R. Winters, Phys. Rev. C **21**, 2190 (1980).
[16]N. M. Larson and F. G. Perey, Oak Ridge National Laboratory Report ORNL/TM-7485 and Report ENDF-297 (unpublished).
[17]G. F. Auchampaugh, Los Alamos Scientific Laboratory Report No. LA-5473-MS, 1974 (unpublished).
[18]M. S. Moore, J. D. Moses, and G. A. Keyworth, Phys. Rev. C **18**, 1328 (1978).
[19]N. Yamamuro, K. Udagawa, and T. Natsume, Nucl. Sci. Eng. **96**, 210 (1987).
[20]C. Y. Fu, Nucl. Sci. Eng. **86**, 344 (1984); **92**, 440 (1986).
[21]D. J. Horen, J. A. Harvey, and N. W. Hill, Phys. Rev. C **24**, 1961 (1981).
[22]C. H. Johnson, Phys. Rev. C **16**, 2238 (1977).
[23]W. Dilg, W. Schantl, H. Vonach, and M. Uhl, Nucl. Phys. **A217**, 269 (1973).
[24]A. Gilbert and A. G. W. Cameron, Can. J. Phys. **43**, 1446 (1965).
[25]M. L. Mehta and F. J. Dyson, J. Math. Phys. **4**, 489 (1963); **4**, 501 (1963).
[26]B. Block and H. Feshbach, Ann. Phys. (N.Y.) **23**, 47 (1963).
[27]C. H. Johnson, *Neutron-Nucleus Collisions A Probe of Nuclear Structure,* AIP Conf. Proc. No. 124, edited by J. Rapaport, R. W. Finlay, S. M. Grimes, and F. S. Dietrich, p. 446 (AIP, New York, 1985), p. 446.
[28]B. K. Arora, D. K. Olsen, P. J. Riley, and C. P. Browne, Phys. Rev. C **10**, 2301 (1974).
[29]P. Luksch and J. W. Tepel, Nucl. Data Sheets **27**, 389 (1979).
[30]D. J. Horen, C. H. Johnson, J. L. Fowler, A. D. MacKellar, and B. Castel, Phys. Rev. C **34**, 429 (1986).
[31]G. A. Keyworth, G. C. Kyker Jr., E. G. Bilpuch, and H. W. Newson, Phys. Lett. **20**, 281 (1966).
[32]E. G. Bilpuch, A. M. Lane, G. E. Mitchell, and J. D. Moses, Phys. Rep. **28**, 145 (1976).